Advancing novel Al-Mn-Cr-Zr based family of alloys tailored for powder bed fusion-laser beam process

(article starts on next page)

Research Article

Advancing novel Al-Mn-Cr-Zr based family of alloys tailored for powder bed fusion-laser beam process

Bharat Mehta [*], Karin Frisk, Lars Nyborg

Department of Industrial & Materials Science, Chalmers University of Technology, Göteborg, Sweden

ARTICLE INFO

ABSTRACT

Additive manufacturing coupled with modern computational tools have enabled novel alloy design possibilities to create materials for the future. One such example is the Al-Mn-Cr-Zr based family of alloys tailored for powder bed fusion-laser beam process. This alloy system has previously been shown to produce crack free samples with good precipitation hardening response and strong thermal stability up to 523 K 2500 h. The current study investigates modifications made to enhance the mechanical response of the alloys. It was done by creating three novel alloy variants with higher Zr and addition of Mg. Interestingly, increasing Zr independently triggered grain refinement while addition of Mg independently causes significant increase in as-printed hardness albeit causing solidification cracking. Desirable properties were achieved when both higher Zr and addition of Mg was done at the same time. As-printed hardness enhanced by 30 % from previously known as-printed hardness of 102 HV to 132 HV in one of the variants. Upon direct ageing, peak hardness of 172 HV is observed thus suggesting retention of precipitation hardening.

1. Introduction

High strength aluminium alloys are extremely sought after due to their exceptional specific strength combined with general corrosion resistance and high recyclability potential. However, there still exists several challenges in a wider adoption of aluminium alloys such as high operating temperatures from currently available 473–493–573 K [1,2]. To make mass adoption possible, it is also important to avoid rare earth elements and critical elements such as Sc, Ce etc. to these alloys. This is where novel processing routes can help achieve the goal of pushing the material property envelope. Additive Manufacturing (AM) could provide the answer to such needs. AM is a relatively new manufacturing technique involving layer by layer material deposition in contrast to cast & wrought manufacturing route which have been around for long [3–5]. Powder bed fusion-laser beam (PBF-LB) is a type of AM route which uses a focused laser beam to selectively melt a small layer of powdered material (metal, polymer etc.), enabling a high cooling rate of 10^3–10^5 K/s [5].

Since both the raw material used (metal powder) and the manufacturing of component (via PBF-LB) involves high cooling rates, thus completely new alloys have been developed in the last few years [6–9]. The main aim has been to develop alloys which are suitable for the process and do not create defects such as solidification cracking. One way is to add elements such as Ti, Zr via ex-situ or in-situ alloying to make the alloys printable. An example of ex-situ alloying is nano functionalization techniques developed to coat Al-powder in order to cause heterogeneous nucleation and make conventional grades of Aluminium alloys printable [8]. Another way has been to avoid cracking altogether and create alloys which are defect tolerant [10,11]. Some authors have leveraged both features together to create high strength Aluminium alloys [6,7,12] reaching yield strengths as high as 500–550 MPa. When it comes to designing high temperature strengths, entirely novel compositions such as Al-Ce-Mn [13], Al-Fe-Cr [9] or Al-Mn-Ni-Cu-Zr [14] have been explored. These alloys reach > 150 MPa yield strengths at temperatures of 573 K, which is quite promising. However, there are two things lacking in the previously done works. The raw materials are fabricated with complex techniques (such as nano functionalization [8]) when similar grain-refinement results could be achieved by relatively simpler direct alloying with Ti/Zr/Sc as shown by [6,14,15]. Additionally, by creating one-two alloy variants, the understanding of such novel alloy systems are limited. Advanced characterisation combined with predicting strengthening of such alloy systems definitely helps in understanding the role of the particular alloy, but it can miss the complicated interactions between different phases and elements present in the

---

alloy. For developing a better understanding of an alloy system such as ours (Al-Mn-Cr-Zr based), creating several variants (ternary, quaternary and quinary) was deemed important.

In our previous work [16,17] we have studied Al-Mn-Cr-Zr family of alloys by creating Al-Mn-Cr, Al-Mn-Zr and Al-Mn-Cr-Zr as three variants, in order to explain the effect of each alloying element clearly. Additionally, it was shown that these alloys are agnostic to the process and are defect tolerant. As-printed hardness > 100 HV combined with precipitation hardening via direct ageing achieved peak hardness > 140 HV for these alloys [18]. Good mechanical properties were observed with yield strength (YS) and ultimate tensile strength (UTS) close to 340 MPa and 440 MPa respectively [19]. However, these strength does not correspond to the strongest aluminium alloys available (up to 500–550 MPa). The value creation aspect of this alloy system would thus be enhanced if higher YS could be realised, combined with a higher thermal stability as has been already shown before [20]. This study has shown to push the boundaries of this alloy system to achieve the abovementioned objective. It has been done by increasing the Zr content during atomisation beyond PBF-LB solubility limit and/or addition of Mg thus creating three new variants of the alloys. Zr increase caused grain refinement and Mg addition enhanced solid solution strength. These variants have been analysed using characterization tools complemented with CALPHAD tools to understand the as-printed microstructure-property relation. The resulting variants were then directly aged at 623 K and 648 K to benchmark against previously known best alloy. This comparison was conducted via microhardness testing.

2. Materials and methods

2.1. Powder

Pre-alloyed spherical powder for this study was fabricated by gas atomization and provided by Höganäs AB, Sweden in particle size distribution of 20–53 μm. Table 1 summarises the chemical compositions of all alloys studied in their as-printed condition based on ICP-OES values conducted at Höganäs AB, Sweden. The trace elements such as O were measured by combustion gas analysis using LECO ON836 and CS844 instruments at Höganäs AB, Sweden. Alloy C from the previous batch of alloys studied before [16] was chosen as a reference alloy for benchmarking purpose.

2.2. PBF-LB processing

All alloys were processed in an EOS M290 machine with 100 μm spot size and 400 W (370 W nominal power) Yb-fiber laser. A full factorial design of experiments (DOE) approach as shown previously [16] was conducted on alloy C and alloy D by varying laser power between 200 and 370 W and laser scan speed between 375 and 2000 mm/s. The optimised processing parameters were chosen as 370 W power, 0.13 mm hatch distance, 1300 mm/s laser speed and 0.03 mm layer thickness with a scan rotation of 67° between each layer. It was seen that > 99.7 % relative bulk density was observed for all four alloys at this parameter, as

further outlined in the results section. This set of parameters was then used to print cubes for all the alloys for microstructure analysis. The cube samples were dimensioned 10 mm each side with a notch to mark gas flow direction, as elucidated in Fig. 1. After printing, the samples were cut with a cold saw from the build plate.

2.3. Simulation software, microstructure evaluation and mechanical testing

All thermodynamics simulations were run using ThermoCalc 2022a software with TCAL8, MOBAL6 databases. The alloy compositions for the simulation were assumed as the ones received from ICP-AES values, and it was supposed that all elements are in solid solution in as-printed state. The samples were cut close to the centre of XZ plane at about 3–4 mm from centre of top plane as shown in Fig. 1 followed by mounting in epoxy-based conductive thermoset resin. The samples were prepared using a Streurs TegraPol 31 machine. The grinding/polishing procedure is explained before [18], which includes grinding with silica grits up to 4000, followed by polishing with 1 μm diamond suspension. A final polishing step for SEM sample preparation was conducted with OP-S silica suspension on a Streurs TegraPol 31 machine. Light optical microscopy was done on a ZEISS Axioscope 7 machine with an automated scale enabling the stitching of images to cover large cross sections. These large cross sections (40–50 mm^2 per sample) were measured at 10X objective to calculate relative density of each sample via image analysis. Image J was used for image analysis. Microstructural evaluation was also done using a Zeiss Gemini 450 SEM equipped with field emission gun source equipped with a six channel back scattered detector. Imaging was done with back scattered electron (BSE). The SEM is fitted with a ULTIM MAX Energy Dispersive X-ray Spectroscopy (EDS) detector from Oxford Instruments, which enabled elemental mapping of microstructure at sub-micron resolutions. For feature analysis done in the Gemini 450 SEM, beam voltage of 5 kV with 1 nA of probe current was chosen with a 30 nm spatial resolution at 5kX magnification to study morphology of precipitates in some of the selected materials. Two random areas of 150 μm × 150 μm each were scanned along build direction (XZ plane) in each alloy. The stitching of images and initial analysis was always conducted in the SEM itself using Aztec software from Oxford Instruments. To plot the data for different test sets, MATLAB or Origin softwares was used. EBSD measurements were conducted on freshly polished samples at 10 kV, 15 nA settings using a Symmetry CMOS EBSD detector from Oxford Instruments. The EBSD data was produced using Aztec v6 from Oxford Instruments and was later processed using Aztec Crystal software. The X-ray diffraction (XRD) of samples was conducted at Höganäs AB on a finely grinded sample (2000 grit size) using a Bragg-Brentano HD X-ray machine with a Cu source (Kα = 1.5406 Å) with 40 mA and 45 kV as the generator settings, scanned between 20–100° 2Θ with a step size of 0.007° and scan step time of 1 s. The heat treatments were conducted in a radiation controlled furnace with temperature control of ± 2 K. The samples were introduced in a
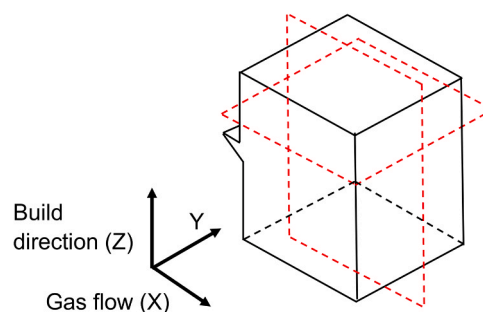
Table 1
Alloy composition for novel Al-Mn-Cr-Zr alloys. All compositions are in wt %. Fe, Si are impurities from the atomisation process.

Alloy name	Variant	Alloy composition (based on ICP-OES)
Alloy C	Zr-low Mg-free	Al 5.0 Mn 0.8 Cr 0.6 Zr 0.0 Mg 0.17 Fe 0.24 Si
Alloy D	Zr-high Mg-free	Al 4.7 Mn 0.8 Cr 1.2 Zr 0.0 Mg 0.13 Fe 0.21 Si
Alloy E	Zr-low Mg-containing	Al 4.7 Mn 0.8 Cr 0.7 Zr 1.0 Mg 0.16 Fe 0.21 Si
Alloy F	Zr-high Mg-containing	Al 4.8 Mn 0.9 Cr 1.1 Zr 1.2 Mg 0.19 Fe 0.20 Si

Fig. 1. Cube design showing the cutting planes for metallographic examination in red and the notch along to mark gas flow direction, based on design developed in [16].

pre-heated furnace and after heat treatments, the samples were air cooled. The Vickers hardness testing was done as per ASTM standards E92, E384 on all the samples. This was conducted using a DuraScan system (from Streurs) keeping a load of 0.3 kg, hold time of 10 s and spacing of at least five times the indentation dimensions. 16 points (4 ×4 grids) were taken along both front planes (XZ) and top plane (XY) of each sample and averaged to get range of hardness for each sample.

3. Results

3.1. Theoretical framework of alloy design

As elucidated in Refs. [16,18], the Al-Mn-Cr-Zr system has been shown to produce crack-free, high density samples. This was made possible following a simplistic alloy design by selecting alloying elements not forming low melting precipitates, as would have been obtained otherwise when alloying with Cu, Mg or Fe. Thus, the alloy system created was shown to have a small solidification range combined with low $\left|\frac{dT}{d(f_s^{\frac{1}{2}})}\right|$ slope close to end of solidification (when $f_s^{\frac{1}{2}} \sim 1$), as represented by Scheil curves, where f_s is the fraction of solid. This method is similar to what is proposed by [21]. Moreover, it has been used for other Al-alloys produced by PBF-LB to show alloy design resistant to solidification cracking [10,11]. This approach made susceptibility to solidification cracking negligible and created so called "inherently crack-free" alloy systems [22]. To add features to the pre-existing material, modifications to the chemistry were introduced as shown in Table 1. Some of the variants were created by increasing Zr beyond PBF-LB solubility limit of ~0.6 wt % to trigger grain refinement [23] (alloy D,F) and further adding Mg (alloy E,F) to trigger solid solution strengthening [24]. Scheil solidification simulation were conducted as shown in Fig. 2a and it suggested that during the beginning of solidification, Zr-rich and

Mn-rich primary precipitation can occur. Rapid solidification during PBF-LB suppresses a large part of this precipitation, thus dissolving most of the Zr in Zr-low variants (alloy C, E) albeit containing some Mn-rich precipitates. Previous studies on alloy C [17] have shown a low amount (<1 area % of precipitates) formed. For the Zr-high variants (alloy D,F), a higher amount of Al_3Zr primary precipitates can form (1.42 vol% instead of 0.78 vol% in Zr-low). Even though PBF-LB can suppress formation of precipitates, primary $L1_2$ cubic Al_3Zr precipitates from the melt and are observed in as-printed condition for Zr-high Al-alloys by others [15,25]. Looking over to the final stage of Scheil solidification, Fig. 2b) and Fig. 3 shows that the solidification path of Mg-containing alloys ends up in a lower temperature Mg-rich eutectic valley. This increases the stability of the liquid while making such alloys susceptible to formation of precipitates such as $Al_{13}Fe_4$, $Al_{15}Si_2M_4$ (M= Fe, Mn, Cr) or Mg_2Si during solidification [8,26]. Segregation of solutes together with formation of primary precipitates and lowering of solidus temperature (see Fig. 3) is suspected to promote the solidification cracking susceptibility of such alloys.

3.1.1. Processability of alloys

Following a similar DOE as explained before [16], the processability window was established for alloys C and alloy D in the EOS M290 machine. A contour plot of relative bulk density in the specimen obtained by varying laser power and laser speed is available in supplementary section. Relative bulk densities in the bulk of the samples as high as 99.7–99.8 % were achieved for both alloys. The optimised processing parameter (mentioned in methods section) was then applied to all alloys and cubes were printed, sectioned, and polished with cross section images shown in Fig. 4. Alloy C and D (Mg-free) showed sub-surface porosity marked with red arrows, which was significantly reduced in alloy E and F (Mg-containing). This porosity was a consequence of choice of processing parameters as contour scanning was deactivated
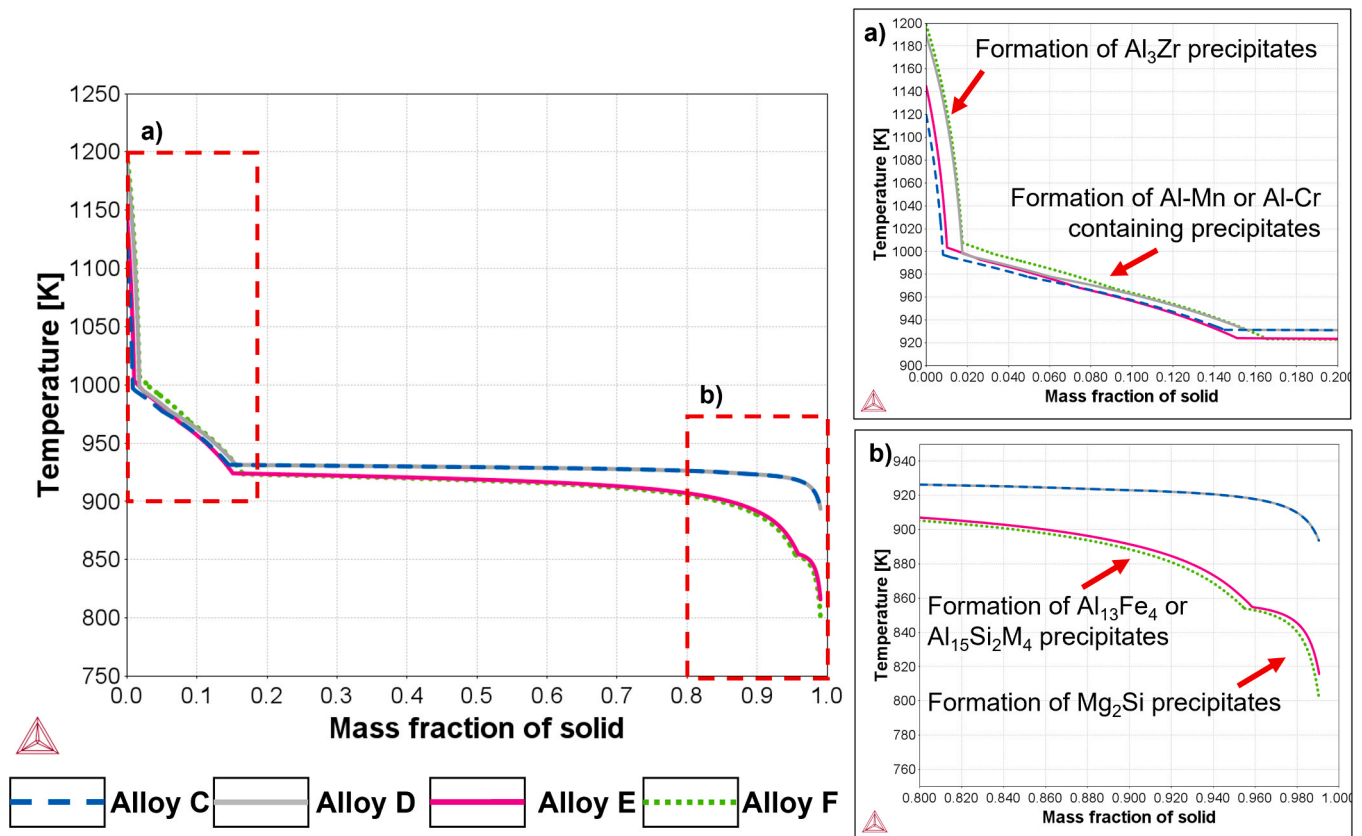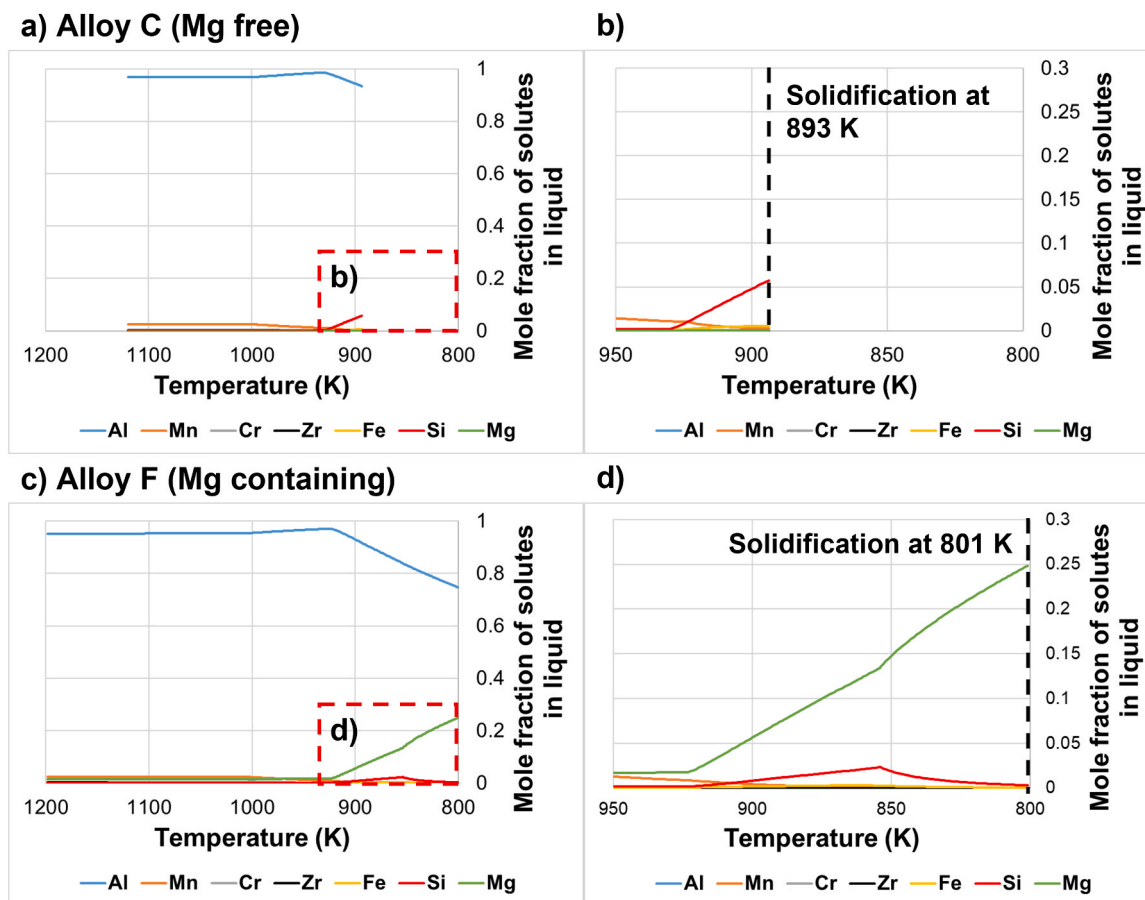

Fig. 2. Scheil solidification simulation for all alloy variants showing formation of different precipitates. The two insets show precipitates during a) starting of solidification (when f_s = 0–0.2) b) end of solidification (when f_s = 0.8–1).

Fig. 3. Scheil solidification simulation conducted for a)-b) Alloy C and c)-d) Alloy F showing the solidification temperatures and segregations of solute in the last liquid for both the alloys.

while printing these samples. Alloy E (Zr-low, Mg-containing) showed solidification cracking as was suspected based on Scheil curves shown in Fig. 2. However, alloy F did not show any solidification cracking, which is discussed later.

3.1.2. Resulting microstructure

The resulting microstructures for all the alloys are summarised in scanning electron micrographs shown in Fig. 5. The microstructure of alloy C processed via EOS M290 machine looks similar as reported before when printed in EOS M100 machine [16,18]. Alloy D and F have significant grain refinement, which is connected to the formation of higher amount of primary L1$_2$ cubic Al$_3$Zr precipitates during solidification, see Fig. 8. Alloy E, which has significant solidification cracking does not seem to have any grain refinement phenomenon. Additionally, as seen in Fig. 5c), most of these cracks seem to originate around the melt pool boundary region of the material.

Fig. 6 summarises the grain size and texture supported with EBSD maps studied for alloy C, D, E and F respectively. It can be seen that a drastic grain refinement is observed with average ECD going from ~26 μm in alloy C → ~1 μm in alloy F, which is more than an order of magnitude. Secondly, grain refinement occurs with a bimodal distribution with high density of refined grains around melt pool boundaries and elongated grains at the surface of melt pool, as has been reported elsewhere [15,27]. Such a strong grain refinement could be responsible for grain size strengthening [18,28].

A deeper investigation into the microstructural differences was conducted for two of the extreme variants (alloy C and F) as shown in Figs. 7 and 8. It revealed that alloy C and alloy F have a similarity in terms of Mn-rich precipitates formed at melt pool boundaries and solidification boundaries as was seen before in alloy C [16]. A higher grain

refinement caused in alloy D and F, combined with higher amounts and sizes of precipitates particularly at melt pool boundaries(compare inset Fig. 7b) and e)). Mg segregations were not seen. The Zr-rich precipitates were seen to have a cubical morphology and were enriched at refined grain regions as reported earlier by others [15,23]. Some of the Mn-rich precipitates were seen to co-precipitate with Zr-rich precipitates as seen in Fig. 8d) [18]. Mg segregations expected in Mg-containing alloy variants were confirmed using electron microscopy. High resolution EDS line scans for Alloy F in as-printed condition (Fig. 9) shows a clear enrichment of Mg, about 6 times higher counts in a small region (~0.1–0.2 μm). While doing the measurements, it was made sure that no other precipitates (such as Mn-rich) were nearby. Slight enrichment of Si, Cr is also seen but the amount is not significant. The final investigation into the microstructure was conducted to quantify the global precipitation in all the four alloys studied. Feature analysis was used to conduct quantitative precipitation analysis across two larger areas of 150 μm × 150 μm each while being able to resolve precipitates up to 0.03 μm. As summarised in Fig. 10a)–d), it can be seen that precipitation increases visibly going from alloy C → alloy D → alloy E → alloy F. When analysing the average equivalent circular diameter (ECD, μm) in Fig. 10d), an increase of about 50 % from 0.1 μm → 0.15 μm. Additionally, the area fraction (Af) of the precipitates also increases from 0.016 → 0.084 which suggests about 5 times increase in Af of precipitates. Most of the increase is suspected from Mn-rich precipitates. Some of the increase could be from primary L1$_2$ Al$_3$Zr precipitates or other Fe-containing or Si-containing precipitates (as suggested in Fig. 2).

3.1.3. Properties

As-printed hardness of the four alloys is summarised in Fig. 11. It is seen that alloy C, E and F have a higher difference in properties along XZ
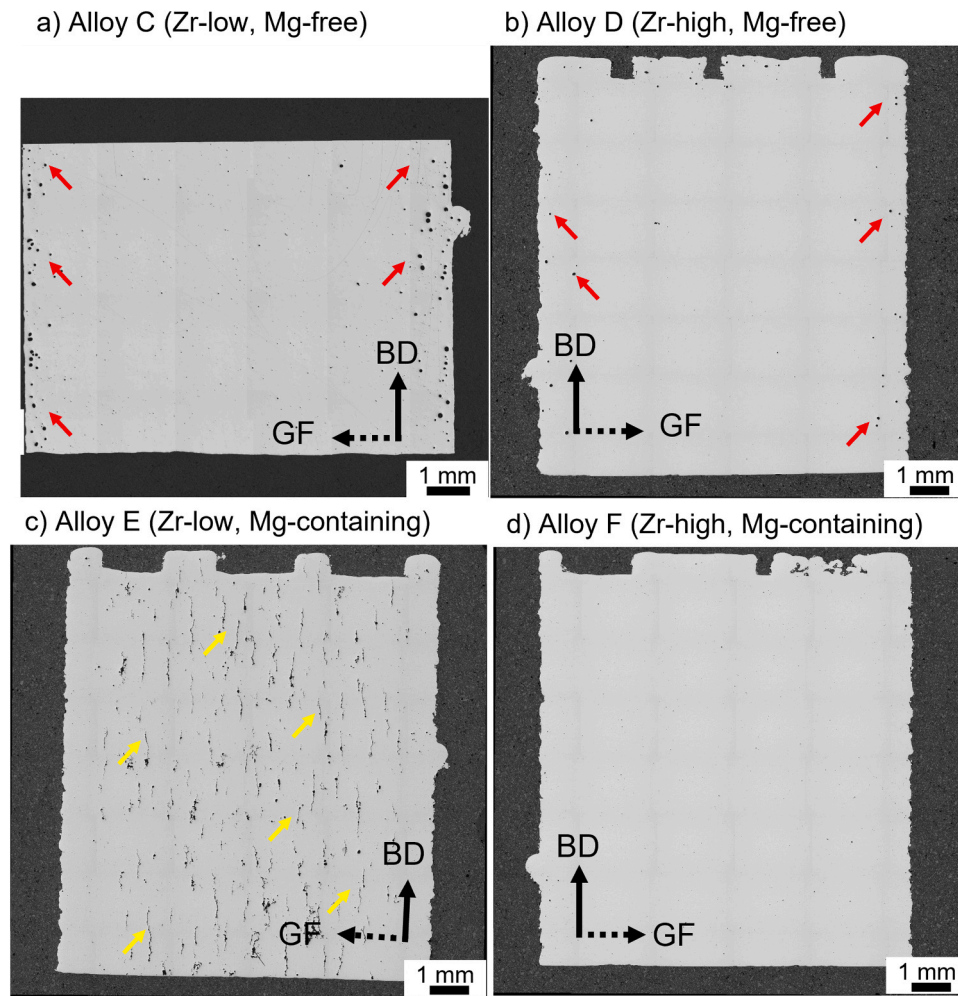
Fig. 4. Optical micrographs showing cut section image along XZ plane with building direction (BD) and gas flow (GF) marked. Alloy C and Alloy D show sub-surface porosity (marked in red) and alloy E shows solidification cracking along BD (marked in yellow).

and XY direction (5.2, 2.9 and 2.8 HV respectively) whereas this difference is reduced for alloy D (1.6 HV). The differences along XZ and XY values are nonetheless lower than 5 %, thus suggesting low anisotropy [29]. Upon comparing alloy C and alloy D, a small increase in average hardness 2.6 HV is observed [28]. The increase in hardness between alloy C and alloy E of 11.8 HV could be attributed mainly to Mg addition to the alloy, thus providing a strong solid solution strengthening effect, albeit causing solidification cracking [16]. A small decrease in grain size combined with increased precipitation between alloy C and alloy E could effect hardness (see Fig. 6 and Fig. 10). The largest increase is observed between alloy C and alloy F, which is 29.7 HV. This difference is expected to be a combination of all effects discussed above, namely grain refinement of primary Al-grains, precipitation hardening Mn-rich precipitates or primary Al_3Zr precipitates) and solid solution effect of Mg.

Finally, alloy C, D, E and F were heat treated via direct ageing at 623 K (0–32 h) and 648 K (0–24 h). The duration and temperatures of heat treatments were selected based on previous studies, wherein peak hardness at 623 K 24 h and 648 K 14 h was observed in alloy C [18]. The same is observed this time after processing alloy C with the EOS M290 machine as shown in Fig. 12. The most important observation is that despite having different starting conditions due to higher precipitation, grain refinement etc., alloy F seems to retain a strong hardening response of about 40 HV, reaching an average peak hardness of 172 HV at 623 K 24 h and 648 K 8 h. Alloy D performs slightly different with peak hardness not reaching the same level as alloy C, rather a faster

hardening response is observed, where peak hardness is achieved in 14 h at 623 K and 4 h at 648 K. Alloy E which is only tested along XZ direction shows a similar hardening response to alloy F and alloy D, wherein the peak is achieved faster than alloy C. For hardness curves at 623 K, the response contains some inconsistencies, which could possibly originate from cracking in the alloy causing micro segregations. Even though the indents were made avoiding solidification cracks, it is possible that regions close to cracks were nonetheless tested.

4. Discussion

In this study, the previously presented Al-Mn-Cr-Zr based alloy system was further extended by increasing Zr beyond solubility and addition of Mg (up to 1.2 wt %) to enhance mechanical properties. Solubility limit of Zr via PBF-LB processing is observed to be around 0.5–0.7 wt % [16,23], thus Zr was increased to double the amount (1–1.2 wt %) to force the formation of primary Al_3Zr precipitates. Mg was further added to the system in limited amounts (1–1.2 wt %) to provide solid solution strengthening. The effect of increasing Zr beyond the solubility shows formation of primary $L1_2$ type cubic Al_3Zr precipitates shown in Fig. 8a), d) owing to the rapid solidification conditions during PBF-LB. The concentration of primary Al_3Zr precipitates is, as expected, observed to be higher in the fine grain region. According to [23,27] this is attributable to the solidification front velocity (v) which increases from melt pool boundaries to the surface of melt pool. This enhances the formation of primary Zr precipitates at melt pool boundaries as opposed to its
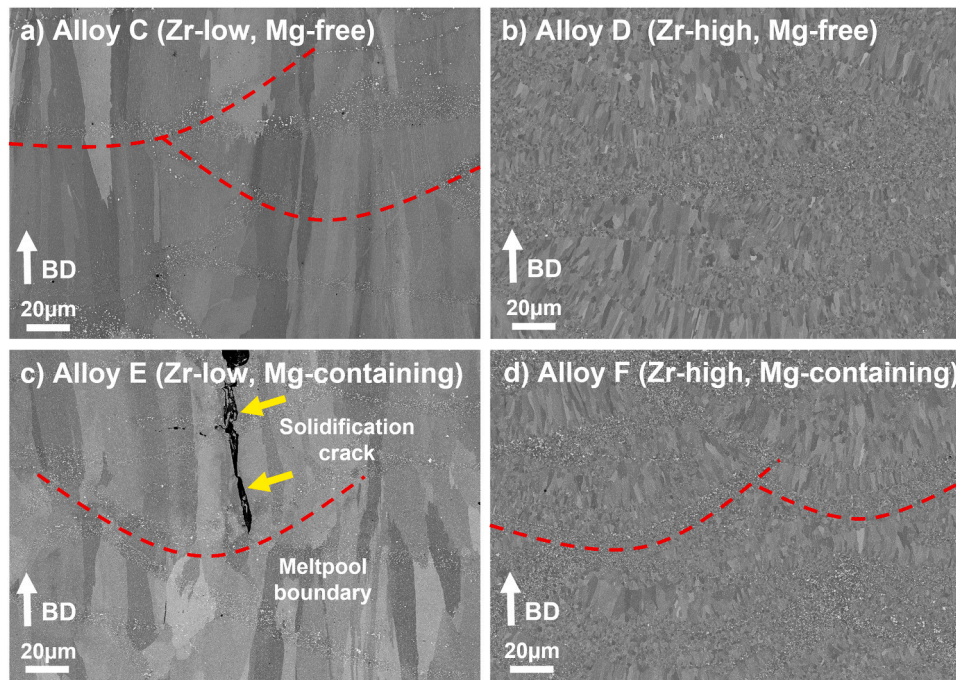
Fig. 5. a)–d) Electron micrographs along XZ plane for all alloy C – alloy F. Building direction (BD) is marked in all the images. The melt pool boundaries are marked in red for illustration and the solidification crack is marked with yellow arrows.

surface, where up to 1.5 wt % Zr can be trapped. The effect of adding Mg is seen with increased hardness in alloy E and F after printing. When comparing as-atomised powder and as-printed samples of Mg-containing variants (alloy E, alloy F), slight evaporation of Mg (0.1 wt % and 0.2 wt % respectively) was observed, which is confirmed by other authors [8,30]. Unlike [15,23,31], the formation of Mg-enriched oxides were not seen in the BSE images taken by us, though their presence cannot be ruled out completely. Upon conducting combustion analysis of all four variants shown in Fig. 13, it became evident that oxygen present in the alloys is reduced after printing consistently for all four variants. Alloy C has a higher starting oxygen content (~1340 ppm) due to it belonging to a different batch of powder not produced at the same time as the next batch of powder (alloy D-F). One reason for negligible MgO could also be due to the oxygen control used by us as compared to others [15,23,27,31] wherein ~0.5–1 wt % O_2 control (5000–10000 ppm) was kept while the EOS M290 machines have a set point of < 0.1 wt % O_2 (<1000 ppm). Having a higher oxygen content in the atomised powder combined with higher process oxygen could result in formation of oxides seen as $MgAl_2O_4$ (spinels) or other Mg-rich oxides. In this case, since the oxygen levels are low to begin with, it is expected that most of the oxides that are formed could have formed as spatter and not end up in the part itself.

The grain refinement effect has several consequences to the alloy system. It creates a randomized texture in the material as confirmed from EBSD measurements done in Fig. 6 and supported with XRD measurements shown in supplementary material. This could lead to isotropic properties when the material is mechanically loaded. As explained by Mishra et al. [32], an ideal Al alloy for PBF-LB process is characterised by three factors namely higher initial rate of formation of constitutionally undercooled zone, wider initial freezing range, and capability of forming potential dispersoids. Solidification cracking resistance, which is most critical is achieved in Al-alloys by having a flat curve at the end of Scheil curve enabled via eutectic solidification or avoiding low melting primary precipitates. This forms the basic principle for alloy design by the authors, such as the ones represented by alloy C, D in Fig. 2. For Mg-containing alloys, which change the solidification conditions by increasing the stability of liquid, thus ending in a low

temperature Mg-rich eutectic valley along with the possibility to formation of several primary precipitates enriched in Fe, Si, Mn/Cr or Mg. This makes the alloy susceptible to cracking. Additionally, Mg-addition or a secondary contour scanning reduces sub-surface porosity (see Fig. 4) and in supplementary section. This phenomenon is not well understood and may need more experimental evidence to explain. Mg segregations occur at solidification boundaries (in this case being a grain boundary) as predicted in Fig. 3 and shown experimentally in Fig. 9. More importantly, such segregations opens up the possibility to form solidification cracks as shown clearly by alloy E. These cracks were seen to originate close to the melt pool boundary region between adjoining Al-grains. This area corresponds to the region of start of solidification after deposition of each layer in PBF-LB process. Fig. 14 suggested these cracked regions were also rich in Mg, which further confirms the observation from Fig. 9 [33,34]. It has also been shown by several authors [7,15,32,35] that pre-alloying with Sc/Zr in high enough amounts leads to formation of primary Al_3Sc/Al_3Zr precipitates in the melt. These precipitates effectively cause heterogeneous nucleation of primary fcc-Al. This reduces the thermal stresses generated during solidification and solidification cracks can be avoided altogether. This explains why alloy F becomes printable as seen in Figs. 4 and 5.

[23,34]As observed qualitatively in Fig. 7, Fig. 8 and later quantitatively in Fig. 10, the concentration of Mn-rich precipitates is increased significantly in the melt pool boundary regions than the surface of melt pools, which is driven by solidification front velocity effect and remelting of layers during PBF-LB process creating a heat affected zone at melt pool boundaries. Interestingly, when the same alloy C was printed in EOS M100 machine [17] at optimum processing parameters (different than the parameters for EOS M290), the ECD and Af was observed to be 0.08 μm and 0.002 respectively which is much less to current 0.1 μm and 0.016 respectively. This difference could be originating from difference in spot sizes of lasers used in both PBF-LB systems (40 μm and 100 μm respectively) effecting the solidification phenomenon for the same material. Fig. 10 shows a small increase in Af between alloy C and alloy D (0.016–0.029), mostly due to increased precipitation at melt pool boundaries. The average size of precipitates is the same. When comparing alloy E, the Af increases from 0.016 to 0.047 between
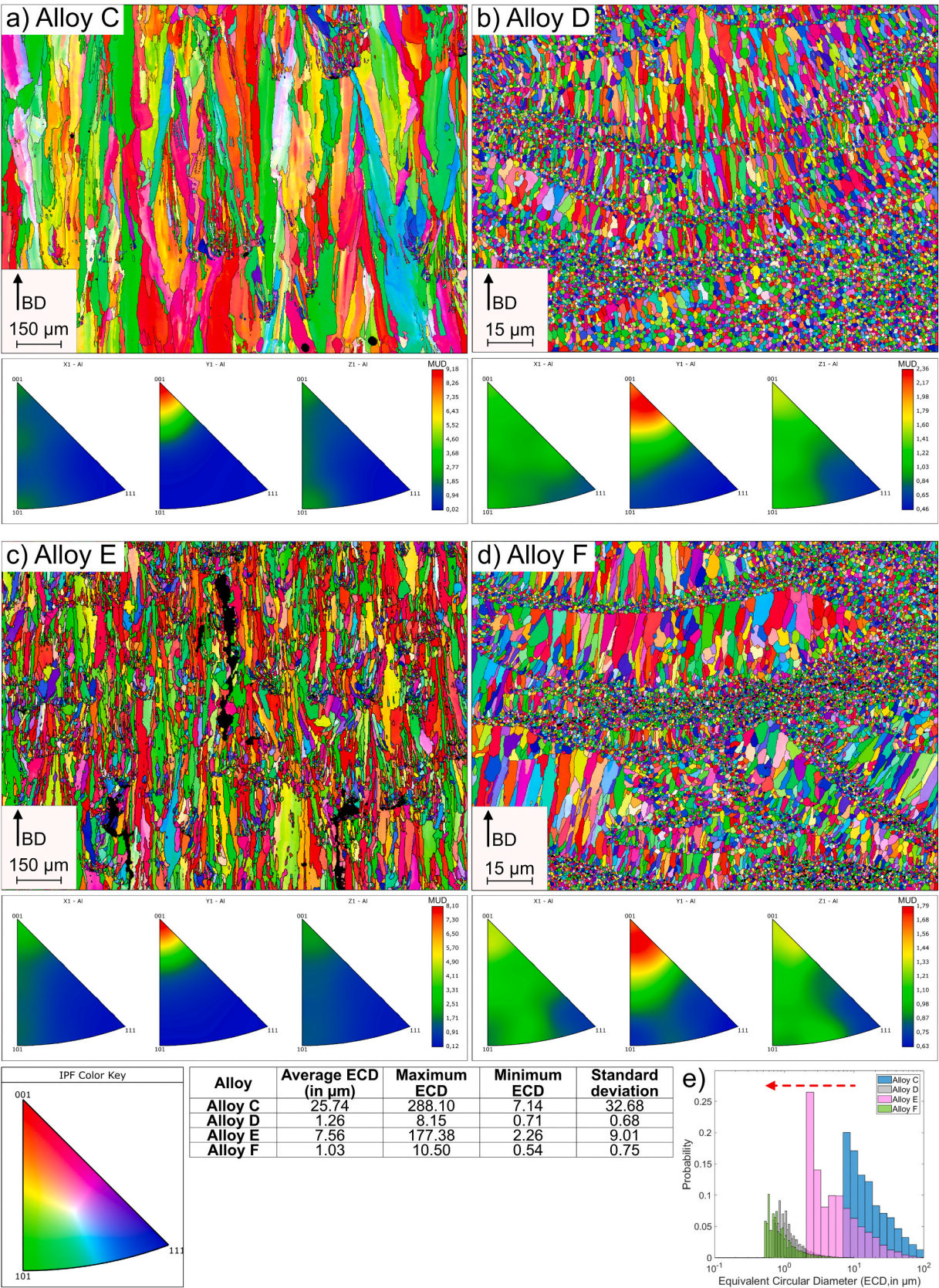
Fig. 6. EBSD inverse pole Fig. X coloured maps for as-printed microstructure along XZ plane in a)-d) Alloy C, D, E and F respectively. Inverse pole figure (IPF) for maps are provided below each map. IPF color key is shown, valid for all the maps. e) shows equivalent circular diameter (ECD, in μm) with the shift in ECD marked with red arrow. The average ECD, in μm together with statistics are provided along with the inverse pole figure for all the maps in a tabular form.
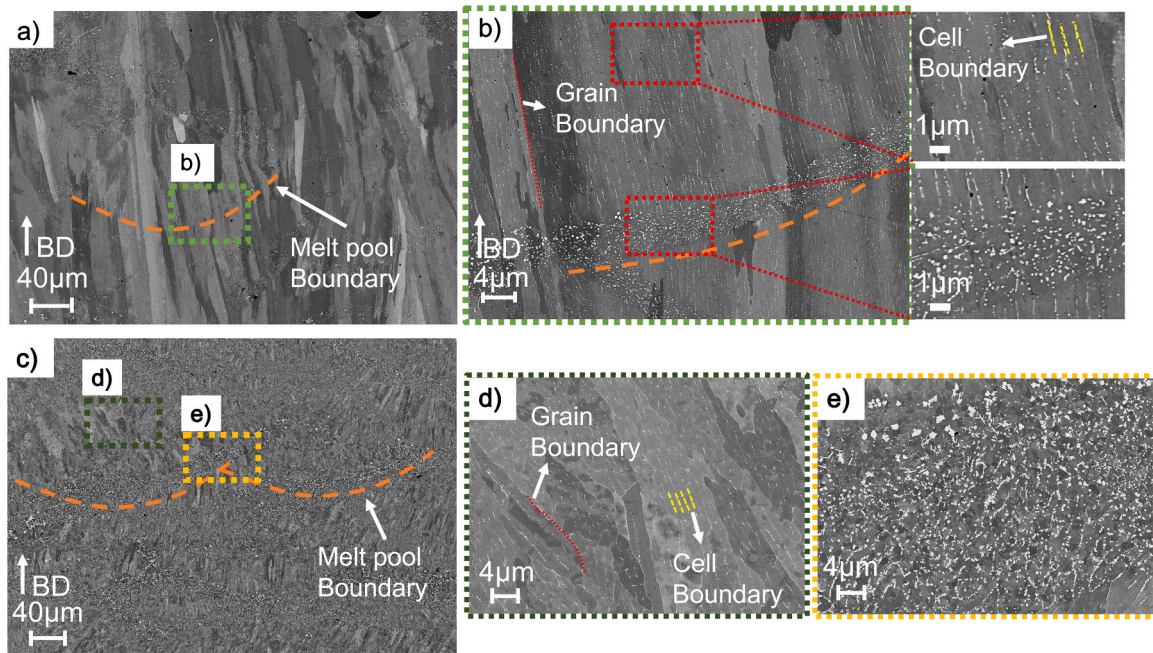
Fig. 7. Electron micrograph for a)-b) alloy C in as-printed condition where different types of precipitates at melt pool boundaries and at solidfication boundaries such as grain/ cell boundaries are shown [16]. c)–e) Shows similar micrographs in alloy F where c) shows an overview of microstructure with insets d),e) showing solidification structures and melt pool boundary structure respectively.
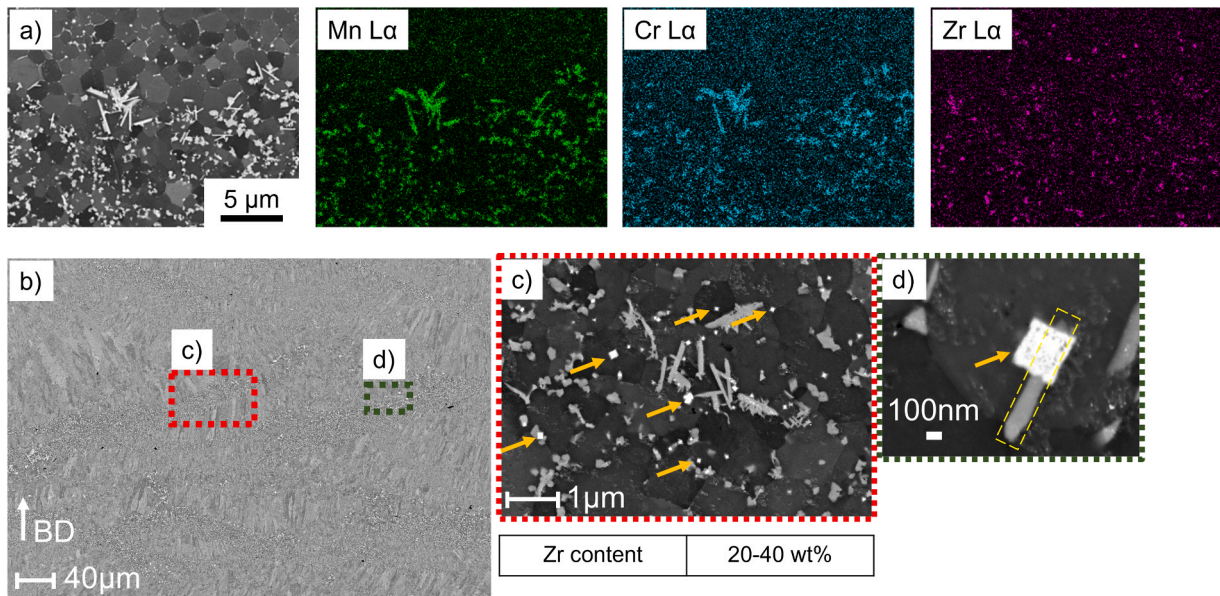

Fig. 8. a) Electron micrograph showing EDS maps in alloy F close to melt pool boundaries which shows segregation of precipitates containing (Mn,Cr) and Zr. No Mg, Si segregations observed b) Similar region in alloy F as shown in inset c), the Zr precipitates (marked in orange arrow) were tested with EDS point scans to show segregation of Zr d) shows a high resolution micrograph showing a needle shaped Mn-rich (possibly Cr-rich) precipitate (yellow) with Zr-rich precipitate (orange) which co-precipitate together.

alloy C and E, which is relatively larger. Moreover, the average size increases (from 0.1 μm to 0.13 μm). In alloy F, the precipitation (Af = 0.084) is significantly high, and the average size increased by ~50 % (~0.15 μm instead of 0.1 μm). Part of the increase is due to primary Al$_3$Zr precipitates and from increased Mn-rich precipitates or tentatively Fe-rich or Si-rich precipitates (from Mg addition). Finer primary Al-grains could contain solutes segregated at solidification boundaries due to solute trapping which could intensify this precipitation. For Mg-containing alloys, we postulate that this Mg effects the solidification path, opening up the possibility for higher precipitation. This could

explain why Fig. 10c)-d) picks up precipitates inside the melt pools unlike alloy C and D. Having higher precipitation is not all bad though. For precipitation hardened alloys, it is best to have higher volume fraction of homogeneously distributed coherent precipitates for the best performance [36]. In this case, sub-micron primary precipitates are formed during printing which could increase as-printed mechanical properties of the alloy in alloy F. However, the 8 % precipitation is still far away from equilibrium state at 648 K (temperature of heat treatment), which would correspond to ~23.4 vol% of total precipitates (~15.3 % of Al-Mn precipitates) in the most alloyed version (alloy F).
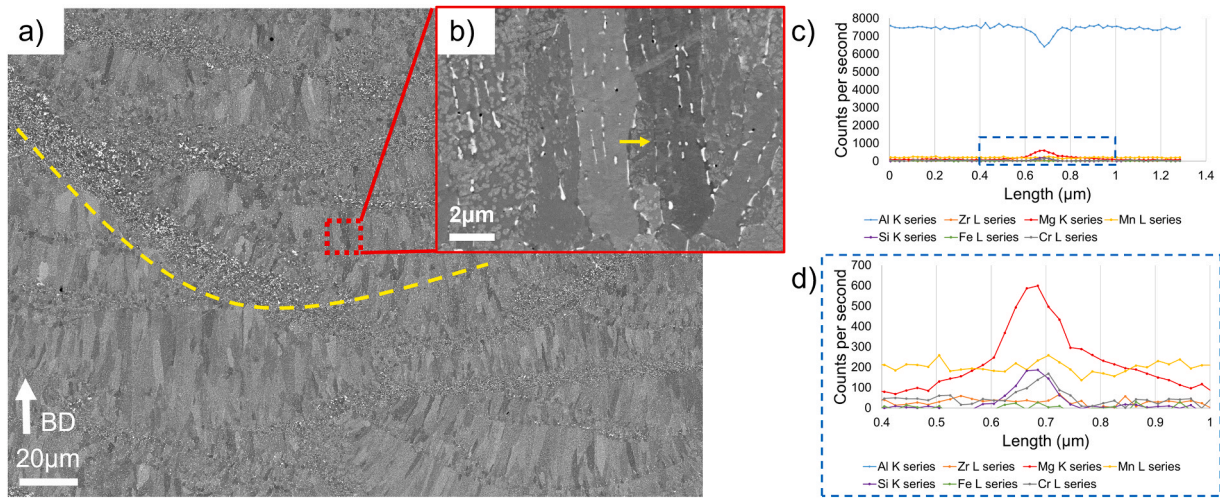
Fig. 9. a) Electron micrograph for alloy F in as-printed condition with melt pool boundaries marked in yellow b) shows inset image at higher resolution where two adjacent grains are visible as BSE contrast where line scan was conducted along the grain boundary (direction shown with yellow line). c)-d) show result from high resolution EDS line scan suggesting primary segregation of Mg with possible segregation of Si, Cr.
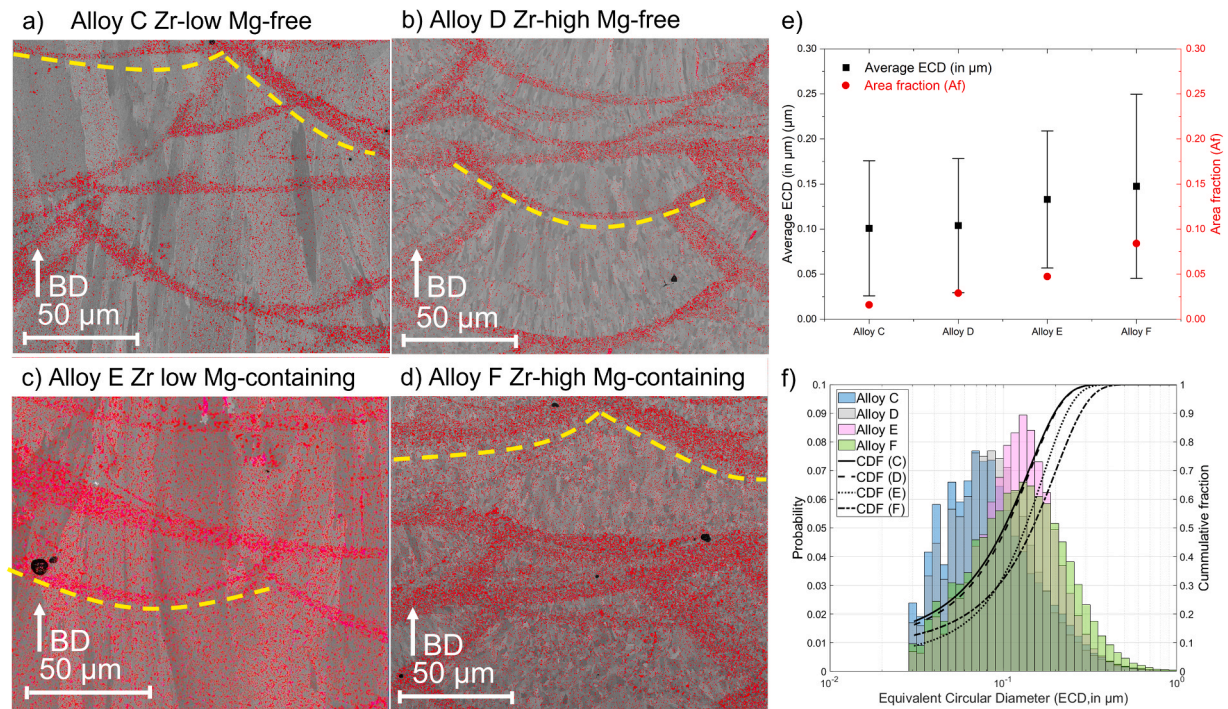
Fig. 10. a)–d) Summary of feature analysis conducted on alloy C, D, E and F respectively shown as electron micrograph showing precipitates marked in red. The melt pool boundaries are demarcated in yellow e) Shows the summary of feature analysis results in terms of equivalent circular diameter and area fraction. Error bars represent one standard deviation f) Cumulative distribution of all the precipitates for the alloys with respect to their equivalent circular diameter.

Hence, there is still opportunity to further harden the alloy via direct ageing. It has been previously shown [18] that the precipitation kinetics in these alloys are not affected by the primary melt pool boundary precipitates. Rather the Mn-rich precipitates contained in the solidification structures such as cell/ grain boundaries are the ones which might control hardening of this alloy system. Al_3Zr nanoprecipitates, which are responsible for the largest strengthening contribution to the matrix are directly affected by Mn-rich precipitation [18]. Nucleation of primary Al_3Zr in melt pool boundaries will lead to depletion of Zr from those regions, thus creating a composite structure wherein the melt pool boundaries have lower Zr than the surface of melt pools. Upon direct ageing, these melt pool boundaries may end up containing lower

amount of Al-Zr nanoprecipitates thus creating a softer structure than the surface of meltpool, which was opposite in the as-printed condition with refined grains hardened with a combination of primary precipitation hardening and grain size effect. The effect of such a composite structure may become visible in tensile specimens, which is part of ongoing work. Additionally, Mg may have a slight effect to increase the stability of the Al_3Zr precipitates in general as it can affect the solubility of elements such as Zr in Al solid solution [37]. EBSD analysis suggest a slight reduction in ECD from 1.3 µm → 1 µm which could be attributable to higher amount of primary Al_3Zr precipitates formed. However, this difference is too small to derive value from and more evidence is needed to validate it. Comparing direct ageing response between alloy C, D, E
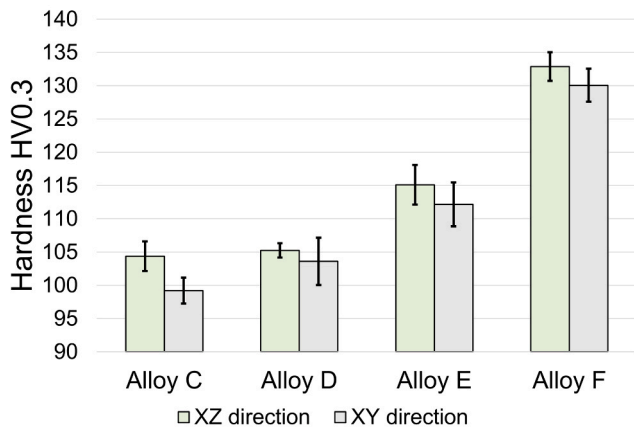
Fig. 11. Vickers hardness HV0.3 for as-printed mechanical properties along XZ and XY direction respectively. Error bars are represented by one standard deviation.

and F at 648 K suggest that peak is achieved in 14 h, 4 h, 8 h and 8 h respectively. The grain refinement and Mg-addition makes the precipitation kinetics faster. In case of alloy D, the peak hardening is slightly reduced to + 35 HV from alloy C (+40 HV). For both alloy E and alloy F, a similar increase of + 40 HV is retained. The final hardness for alloy F is 172 HV, which suggests high-strength.

Finally, the creation of these alloys having fewer elements with a large range of properties (between 85 HV – 170 HV) make the alloy system desirable for several applications. The alloys are free from any rare earth and critical elements such as Sc, Ce, Co etc. making them lucrative for mass-production applications. The alloys are designed for a high thermal stability up to 523–573 K of operating temperatures [2, 38]. One part of thermal stability which is isothermal long term thermal stability has been shown previously by the authors, wherein the alloy C did not lose any hardness after ageing at 523 K 2500 h. When ageing at 623 K for 1000 h, there was a drop in hardness only after 200 h and a total drop of 17–18 HV (13 % of hardness) was observed. The other variants should behave in a similar manner, which means alloy F may retain ~140–150 HV hardness after isothermal ageing at 623 K 1000 h. Another proven feature with these alloys is the simpler heat treatments, wherein a usual T6 type of heat treatment [39] can be skipped and a T5 type of direct ageing treatment can be adopted as is suggested by others [12]. After conducting several experiments, it has been established that

slow coarsening precipitates are responsible for a stable heat treatment response in these alloys, which translates to shorter and easier heat treatment, especially on complex components. A complex component with varying surfaces and thick/thin sections could be hard to heat treat if there is sensitivity of heat treatment to cooling rates when taken out of furnace. For these alloys, it does not seem to be the case and similar results are observed when quenched or air cooled the samples [16,18]. Table 2 shows an overall summary of hardness response of several Al-alloys studied by other researchers. It can be seen that this novel Al-Mn-Cr-Zr-Mg family of alloys produce one of the best responses combined with a high versatility.

5. Conclusions

Advancement to the pre-established Al-Mn-Cr-Zr family of alloys tailored for PBF-LB process has been shown. The new variants with increased Zr content and addition of Mg showed high as-printed hardness of 132 HV in the most alloyed version (alloy F). Addition of Mg alone caused solidification cracking (alloy E) and was balanced by increasing Zr content (alloy F). As a result, heavy grain refinement with bimodal grain distribution is caused leading to tentative isotropic properties. Direct ageing response reveal faster precipitation kinetics than previously established in alloy C. The amount of hardening via direct ageing in alloy F was similar to alloy C (40 HV) making the peak hardness reach 172 HV after ageing 623 K 24 h and 648 K 8 h, which
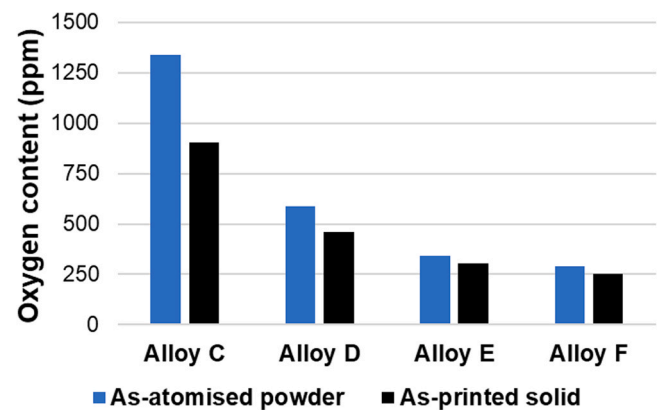

Fig. 13. Oxygen content in as-atomised powder and as-printed solid for all four variants. Testing done by combustion gas analysis.
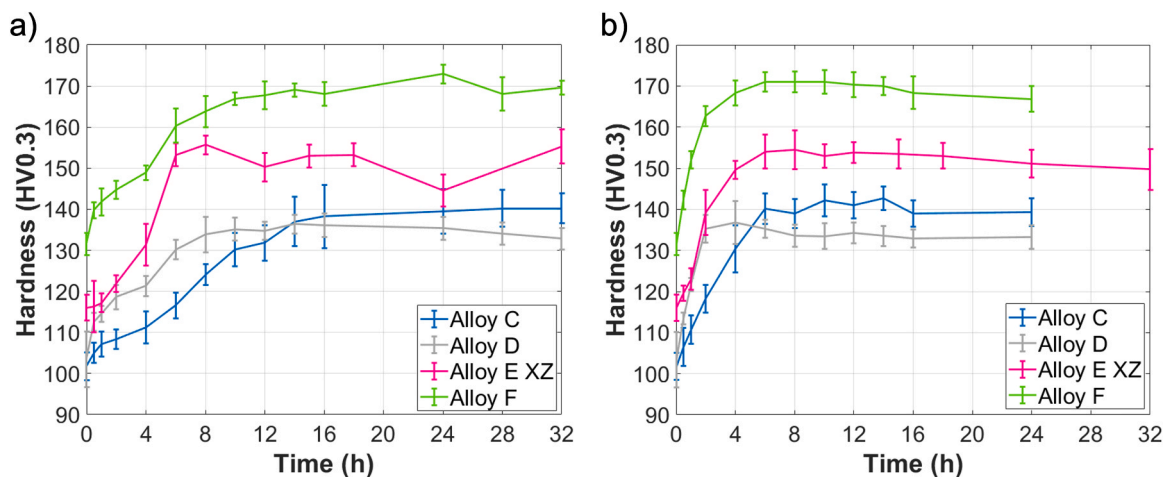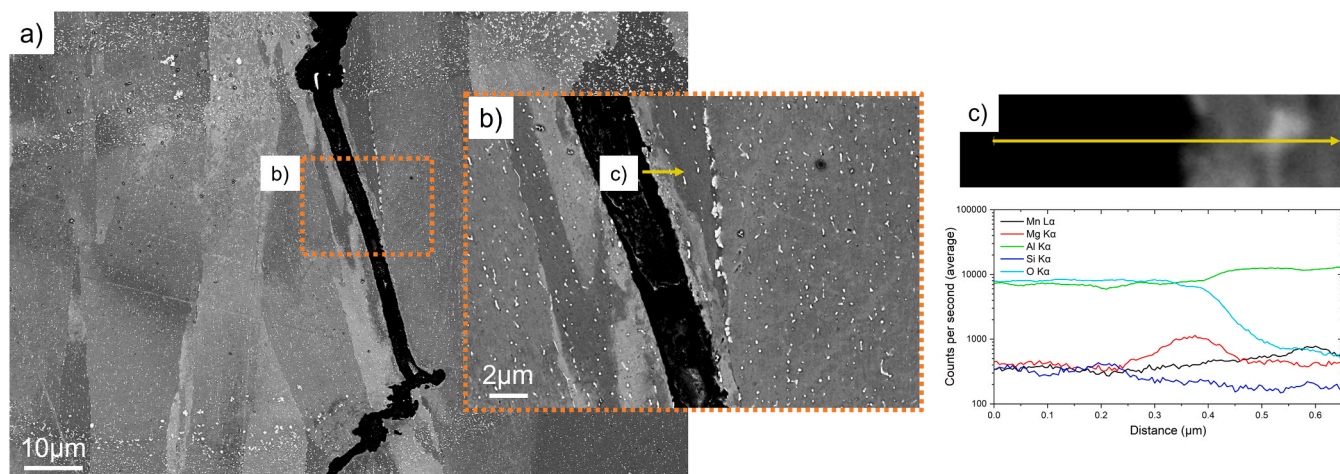

Fig. 12. Direct ageing response on alloy C, D, E and F at a) 623 K (0–32 h) and b) 648 K (0–24 h) respectively. Hardness data for alloy C, D and F is averaged for XZ and XY directions and error bars of one standard deviation is shown. For alloy E, only data along XZ direction was obtained. The error bar represents one standard deviation.

Fig. 14. a) Electron micrograph for alloy E in as-printed condition focusing on a solidification crack b) Shows inset image at higher resolution where solidification crack is visible where line scan (c)) was conducted along the crack boundary (direction shown with yellow line) c) Show result from high resolution EDS line scan suggesting segregation of Mg at the edge of the crack. Note: logarithmic scale used in Y-axis.

Table 2
Summary of hardness response of various Al-alloys.

Alloy composition/name	Condition	Hardness	Reference
Al-Mn-Cr-Zr (Alloy C)	As-printed	102	[18]
	Aged 648 K 14 h	143	
Al-Mn-Cr-Zr-Mg (Alloy F)	As-printed	132	This work
	Aged 648 K 8 h	172	
AlSi10Mg	As-printed	124	[40]
	Aged 573 K 2 h	82	
Al-Mg-Sc-Zr (Scalmalloy®)	As-printed	105–113	[6,41]
	Aged 598 K 4 h	172–177	
Al-Mg-Zr (Addalloy®)	As-printed	89–98	[15]
	Aged 673 K 8 hh	134	
Al-Mn-Mg-Sc-Zr	As-printed	140	[42]
	Aged 573 K 5 h	186	
Al-7075 +ZrH$_2$ (Nano functionalized)	As-printed	-	[8]
	T6: 753 K 2 h + 393 K 18 h	137	
Al-Ce-Mn	As-printed	180	[13]
Al12Si0.75Mg	As-printed	149	[43]
	Aged 573 K 3 h	110	
Al-Fe-Cr	As-printed	160–190	[9]
Al-Mn-Ni-Cu-Zr	As-printed	125	[14]
	Aged 673 K 1 h	160	

suggests a tentative UTS of 500–550 MPa. Such a systematic alloy design has enabled the authors to offer an alloy system which has high density (~99.8 %), crack free, rare-earth element free and high strength with high thermal stability. These alloy systems could thus help advance additive manufacturing technologies towards mass production use in the future.

CRediT authorship contribution statement

Bharat Mehta: Conceptualization, Methodology, Investigation, Writing – original draft, Project administration. **Karin Frisk:** Conceptualization, Methodology, Investigation, Data curation, Writing – review & editing, Supervision. **Lars Nyborg:** Conceptualization, Data curation, Funding acquisition, Writing – review & editing, Supervision.

Declaration of Competing Interest

The authors declare that they have no known competing financial interests or personal relationships that could have appeared to influence the work reported in this paper.

References

[1] ASM International, Introduction to Aluminum and Aluminum Alloys, Metals Handbook Desk Edition, 1998, pp. 417–423, https://doi.org/10.31399/asm.hb. v02.9781627081627.

[2] J.L. Cann, et al., Sustainability through alloy design: challenges and opportunities, Prog. Mater. Sci. 117 (July 2020) (2021), 100722, https://doi.org/10.1016/j. pmatsci.2020.100722.

[3] D.D. Gu, W. Meiners, K. Wissenbach, R. Poprawe, Laser additive manufacturing of metallic components: materials, processes and mechanisms, Int. Mater. Rev. 57 (3) (2012) 133–164, https://doi.org/10.1179/1743280411Y.0000000014.

[4] A. 52900:2015, Standard Terminology for Additive Manufacturing – General Principles – Terminology, ASTM International i, 2015, pp. 1–9 ([Online]. Available), ⟨http://compass.astm.org/EDIT/html_annot.cgi?ISOASTM52900+15⟩.

[5] T. DebRoy, et al., Additive manufacturing of metallic components – process, structure and properties, Prog. Mater. Sci. 92 (2018) 112–224, https://doi.org/ 10.1016/j.pmatsci.2017.10.001.

[6] K. Schmidtke, F. Palm, A. Hawkins, C. Emmelmann, Process and mechanical properties: applicability of a scandium modified Al-alloy for laser additive manufacturing, Phys. Procedia 12 (PART 1) (2011) 369–374, https://doi.org/ 10.1016/j.phpro.2011.03.047.

[7] Q. Jia, et al., Selective laser melting of a high strength Al[sbnd]Mn[sbnd]Sc alloy: Alloy design and strengthening mechanisms, Acta Mater. 171 (2019) 108–118, https://doi.org/10.1016/j.actamat.2019.04.014.

[8] J.H. Martin, B.D. Yahata, J.M. Hundley, J.A. Mayer, T.A. Schaedler, T.M. Pollock, 3D printing of high-strength aluminium alloys, Nature 549 (7672) (2017) 365–369, https://doi.org/10.1038/nature23894.

[9] M.T. Perez-Prado, A. Martin, D.F. Shi, and S. Milenkovic, An Al-5Fe-6Cr alloy with outstanding high temperature mechanical behavior by laser powder bed fusion, 55 (January), 2022. ⟨https://doi.org/10.1016/j.addma.2022.102828⟩.

[10] S. Thapliyal, et al., An integrated computational materials engineering-anchored closed-loop method for design of aluminum alloys for additive manufacturing,

Materials 9 (December 2019) (2020), 100574, https://doi.org/10.1016/j.mtla.2019.100574.

[11] A. Dreano, J. Favre, C. Desrayaud, P. Chanin-Lambert, A. Wimmer, M.F. Zaeh, Computational design of a crack-free aluminum alloy for additive manufacturing, Addit. Manuf. 55 (2022), https://doi.org/10.1016/j.addma.2022.102876.

[12] P.A. Rometsch, Y. Zhu, X. Wu, A. Huang, Review of high-strength aluminium alloys for additive manufacturing by laser powder bed fusion, Mater. Des. 219 (2022), 110779, https://doi.org/10.1016/j.matdes.2022.110779.

[13] A. Plotkowski, et al., Microstructure and properties of a high temperature Al–Ce–Mn alloy produced by additive manufacturing, Acta Mater. 196 (2020) 595–608, https://doi.org/10.1016/j.actamat.2020.07.014.

[14] M. Buttard, et al., Multi-scale microstuctural investigation of a new Al-Mn-Ni-Cu-Zr aluminium alloy processed by laser powder bed fusion, Materials 18 (July) (2021), 101160, https://doi.org/10.1016/j.mtla.2021.101160.

[15] J.R. Croteau, et al., Microstructure and mechanical properties of Al-Mg-Zr alloys processed by selective laser melting, Acta Mater. 153 (2018) 35–44, https://doi.org/10.1016/j.actamat.2018.04.053.

[16] B. Mehta, L. Nyborg, K. Frisk, E. Hryha, Al–Mn–Cr–Zr-based alloys tailored for powder bed fusion-laser beam process: Alloy design, printability, resulting microstructure and alloy properties, J. Mater. Res. 3 (2022) 1–13, https://doi.org/10.1557/s43578-022-00533-1.

[17] A. Martucci, B. Mehta, M. Lombardi, L. Nyborg, The influence of processing parameters on the Al-Mn enriched nano-precipitates formation in a novel Al-Mn-Cr-Zr alloy tailored for power bed fusion-laser beam process, Metals 12 (8) (2022), https://doi.org/10.3390/met12081387.

[18] B. Mehta, K. Frisk, L. Nyborg, Effect of precipitation kinetics on microstructure and properties of novel Al-Mn-Cr-Zr based alloys developed for powder bed fusion – laser beam process, J. Alloy. Compd. (2022), https://doi.org/10.1016/j.jallcom.2022.165870.

[19] S. Bengtsson, B. Mehta, K. Frisk, L. Nyborg, New aluminium alloy tailored for powder bed fusion – laser beam process, World 2022 Congr. Exhib.: Conf. Proc. (2022).

[20] B. Mehta, K. Frisk, L. Nyborg, S. Bengtsson, E. Hryha, Thermal stability In Al-Mn-Cr-Zr based aluminium alloys tailored for powder bed fusion – laser beam, World 2022 Congr. Exhib.: Conf. Proc. (2022).

[21] S. Kou, A criterion for cracking during solidification, Acta Mater. 88 (2015) 366–374, https://doi.org/10.1016/j.actamat.2015.01.034.

[22] B. MEHTA, High Performance Aluminium Alloys for Laser Powder Bed Fusion: Alloy Design and Development, p. 48, 2021, [Online]. Available: ⟨https://www.chalmers.se/sv/institutioner/ims/kalendarium/Sidor/High-Performance-Aluminium-Alloys-for-Laser-Powder.aspx %0Ahttps://research.chalmers.se/publication/527075/file/527075_Fulltext.pdf⟩.

[23] S. Griffiths, M.D. Rossell, J. Croteau, N.Q. Vo, D.C. Dunand, C. Leinenbach, Effect of laser rescanning on the grain microstructure of a selective laser melted Al-Mg-Zr alloy, Mater. Charact. 143 (November 2017) (2018) 34–42, https://doi.org/10.1016/j.matchar.2018.03.033.

[24] T. Uesugi, K. Higashi, First-principles studies on lattice constants and local lattice distortions in solid solution aluminum alloys, Comput. Mater. Sci. 67 (2013) 1–10, https://doi.org/10.1016/j.commatsci.2012.08.037.

[25] A. Mehta, et al., Additive manufacturing and mechanical properties of the dense and crack free Zr-modified aluminum alloy 6061 fabricated by the laser-powder bed fusion, Addit. Manuf. 41 (November 2020) (2021), 101966, https://doi.org/10.1016/j.addma.2021.101966.

[26] T. Böllinghaus, H. Herold, C. Cross, and J. Lippold, Hot Cracking Phenomena in Welds II. 2008. Accessed: Jul. 28, 2022. [Online]. Available: ⟨https://link.springer.com/book/10.1007/978-3-540-78628-3⟩.

[27] A.B. Spierings, K. Dawson, P.J. Uggowitzer, K. Wegener, Influence of SLM scan-speed on microstructure, precipitation of Al3Sc particles and mechanical properties in Sc- and Zr-modified Al-Mg alloys, Mater. Des. (2018), https://doi.org/10.1016/j.matdes.2017.11.053.

[28] Z.C. Cordero, B.E. Knight, C.A. Schuh, Six decades of the Hall–Petch effect – a survey of grain-size strengthening studies on pure metals, Int. Mater. Rev. 61 (8) (2016) 495–512, https://doi.org/10.1080/09506608.2016.1191808.

[29] A.B. Spierings, K. Dawson, K. Kern, F. Palm, K. Wegener, SLM-processed Sc- and Zr-modified Al-Mg alloy: mechanical properties and microstructural effects of heat treatment, Mater. Sci. Eng. A 701 (June) (2017) 264–273, https://doi.org/10.1016/j.msea.2017.06.089.

[30] L. Deillon, F. Jensch, F. Palm, M. Bambach, A new high strength Al–Mg–Sc alloy for laser powder bed fusion with calcium addition to effectively prevent magnesium evaporation, J. Mater. Process Technol. 300 (2022), 117416, https://doi.org/10.1016/j.jmatprotec.2021.117416.

[31] A.B. Spierings, et al., Microstructural features of Sc- and Zr-modified Al-Mg alloys processed by selective laser melting, Mater. Des. 115 (2017) 52–63, https://doi.org/10.1016/j.matdes.2016.11.040.

[32] R.S. Mishra, S. Thapliyal, Design approaches for printability-performance synergy in Al alloys for laser-powder bed additive manufacturing, Mater. Des. 204 (2021), 109640, https://doi.org/10.1016/j.matdes.2021.109640.

[33] J.P. Oliveira, A.D. LaLonde, J. Ma, Processing parameters in laser powder bed fusion metal additive manufacturing, Mater. Des. 193 (2020) 1–12, https://doi.org/10.1016/j.matdes.2020.108762.

[34] A. Durga, et al., Grain refinement in additively manufactured ferritic stainless steel by in situ inoculation using pre-alloyed powder, Scr. Mater. 194 (2021), 113690, https://doi.org/10.1016/j.scriptamat.2020.113690.

[35] N. Qbau, N.D. Nam, N.X. Ca, N.T. Hien, The crack healing effect of scandium in aluminum alloys during laser additive manufacturing, J. Manuf. Process 50 (2020) 241–246, https://doi.org/10.1016/j.jmapro.2019.12.050.

[36] K.E. Easterling, D.A. Porter, Phase Transformations in Metals and Alloys, Second. London: Chapman & Hill, 1992.

[37] M. Roscher, Development of high-strength Aluminum alloys for Laser Powder Bed Fusion, 2022.

[38] R.A. Michi, A. Plotkowski, A. Shyam, R.R. Dehoff, S.S. Babu, Towards high-temperature applications of aluminium alloys enabled by additive manufacturing, Int. Mater. Rev. (2021), https://doi.org/10.1080/09506608.2021.1951580.

[39] T.H.E. Major, A. Alloy, Heat Treatment Practices of Age-hardenable Aluminum Alloys, 2016, https://doi.org/10.31399/asm.hb.v04e.a0006288.

[40] AlSi10Mg material datasheet: SLM Solutions. https://www.slm-solutions.com/fileadmin/Content/Powder/MDS/MDS_Al-Alloy_AlSi10Mg_0520_EN.pdf (Accessed 05 August 2022).

[41] B. Mehta, A. Svanberg, L. Nyborg, Laser powder bed fusion of an al-mg-sc-zr alloy: manufacturing, peak hardening response and thermal stability at peak hardness, Metals 12 (1) (2022), https://doi.org/10.3390/met12010057.

[42] Q. Jia, et al., Precipitation kinetics, microstructure evolution and mechanical behavior of a developed Al–Mn–Sc alloy fabricated by selective laser melting, Acta Mater. 193 (2020) 239–251, https://doi.org/10.1016/j.actamat.2020.04.015.

[43] Y. Bai, Y. Yang, Z. Xiao, M. Zhang, D. Wang, Process optimization and mechanical property evolution of AlSiMg0.75 by selective laser melting, Mater. Des. 140 (2018) 257–266, https://doi.org/10.1016/j.matdes.2017.11.045.